



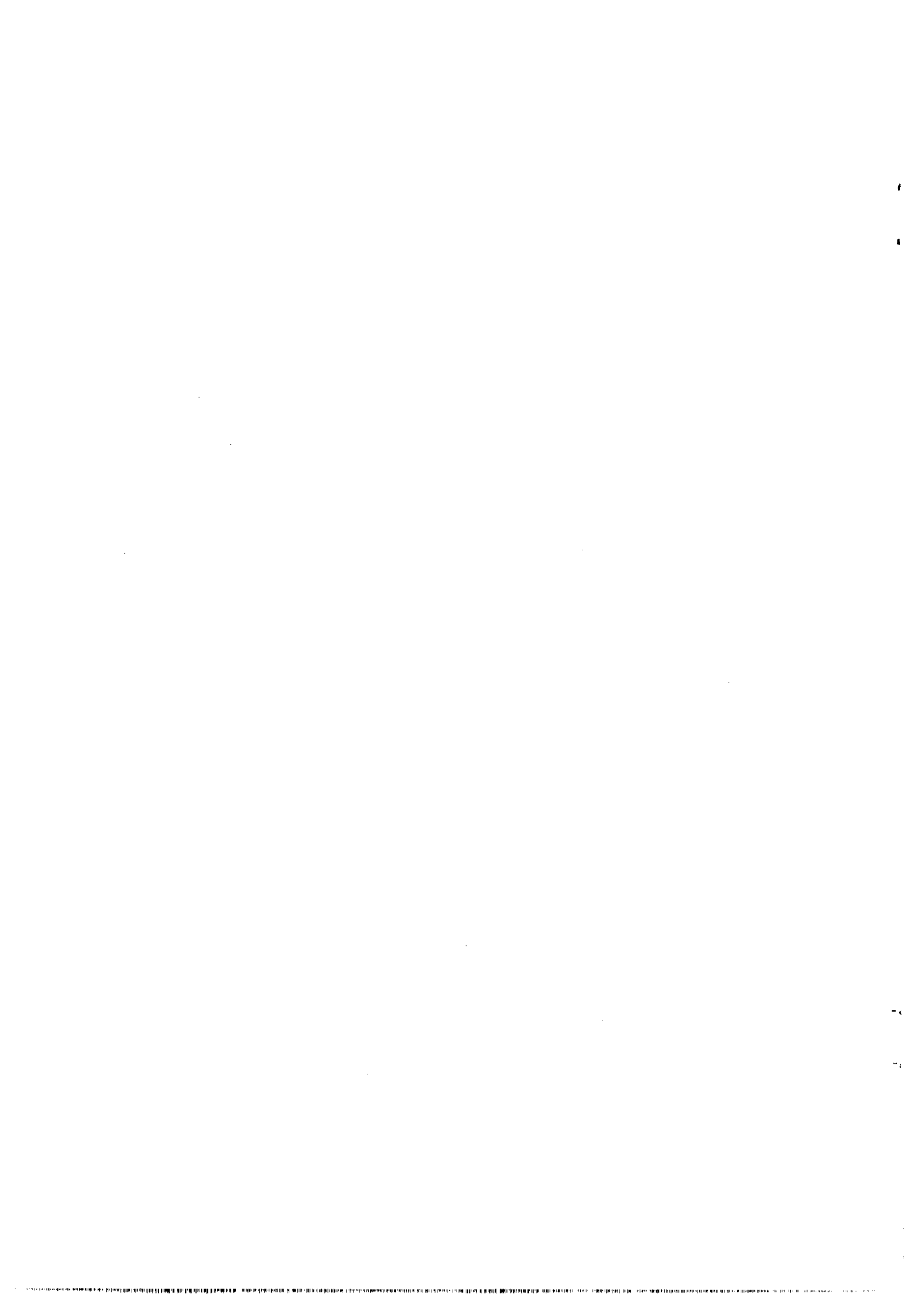
INCLUSIVE VECTOR-MESON PRODUCTION IN THE
CENTRAL REGION OF pp COLLISIONS AT $\sqrt{s} = 63$ GeV

The Axial Field Spectrometer Collaboration

T. Åkesson⁴, M.G. Albrow⁶, S. Almedhed⁴, O. Benary⁷, H. Bøggild³, O. Botner², H. Brody⁵,
V. Burkert², A. di Ciaccio¹, D. Cockerill⁶, S. Dagan⁷, E. Dahl-Jensen³, I. Dahl-Jensen³,
P. Dam³, G. Damgaard³, W.M. Evans⁶, C.W. Fabjan², T. Ferbel², P. Frandsen², S. Frankel⁵,
W. Frati⁵, M.D. Gibson⁶, H. Gordon¹, A. Hallgren², K.H. Hansen³, B. Heck², S. Henning⁴,
J.W. Hiddleston⁶, H.J. Hilke², R. Hogue¹, J.E. Hooper³, G. Jarlskog⁴, P. Jeffreys²,
G. Kessler², T. Killian¹, J. v.d. Lans², P.R. Lindblom⁵, J. Lindsay², D. Lissauer⁷,
E. Lohse³, B. Lörstad⁴, H.J. Lubatti², T. Ludlam¹, N.A. McCubbin⁶, A. Melin⁴, U. Mjörnmark⁴,
R. Møller³, W. Molzon⁵, B.S. Nielsen², S.Ø. Nielsen³, A. Nilsson⁴, L.H. Olsen², Y. Oren⁷,
L. Rosselet², E. Rosso², A. Rudge², R.H. Schindler², B. Schistad³, D.W. Wang^{2*},
Ch.J. Wang^{2*}, W.J. Willis², M. Winik¹, W. Witzeling² and C. Woody¹

- 1) Brookhaven National Laboratory, Upton, USA
- 2) CERN, Geneva, Switzerland
- 3) Niels Bohr Institute, Copenhagen, Denmark
- 4) University of Lund, Sweden
- 5) University of Pennsylvania, Philadelphia, USA
- 6) Rutherford Appleton Laboratory, Didcot, UK
- 7) University of Tel Aviv, Israel
- *) Visitor from Beijing University, China

(Submitted to Nuclear Physics B)



ABSTRACT

Production of ρ^0 , K^{*0} , \bar{K}^{*0} , and ϕ have been measured in proton-proton collisions at the CERN Intersecting Storage Rings (ISR) at low p_T in the central region. Their rapidity distributions are all consistent with being flat for $|y| < 1$. The transverse mass spectra are well described by $\exp(-a\mu_T)$, with $a = -6.4 \pm 0.2 \text{ GeV}^{-1}$. The cross-sections for $d\sigma/dy|_{y=0}$ are $6.5 \pm 0.8 \pm 1.2 \text{ mb}$ for ρ^0 , $1.9 \pm 0.3 \pm 0.3 \text{ mb}$ for K^{*0} , $1.9 \pm 0.3 \pm 0.3 \text{ mb}$ for \bar{K}^{*0} , and $0.60 \pm 0.12 \pm 0.13 \text{ mb}$ for ϕ , where the first error is statistical and the second is systematic.



1. INTRODUCTION

We have measured inclusive vector-meson spectra at the CERN Intersecting Storage Rings (ISR) at $\sqrt{s} = 63$ GeV for $|y| < 1$ and transverse momentum (p_T) up to 1.5 GeV/c. Experimental data for vector mesons are relatively scarce at these energies, in particular in the central region [1]. At lower energies, however, their production has been more systematically investigated [2].

Previous results indicate that in high-energy hadron collisions vector-meson production dominates over the production of pseudoscalar mesons. This is in qualitative agreement with spin statistics [3] which predict that most observed particles are decay products of vector-meson resonances. More detailed quark-parton models give quantitative predictions on the behaviour of vector-meson production [4]. Furthermore, it is of interest to know how much of the short-range correlations in hadron collisions can be explained by vector mesons.

The paper is organized as follows. In Sections 2 and 3 we describe the apparatus and the data analysis, and in Section 4 the results are given.

2. EXPERIMENTAL SET-UP

The experiment was performed using the Axial Field Spectrometer (AFS) shown in fig. 1. The magnet provides an azimuthally symmetric field of ~ 0.5 T over the central region containing the track chambers. These cylindrically symmetric drift chambers are divided into two parts, to accommodate supports for the beam pipe. They are 1.42 m in length, and extend radially from 0.20 to 0.80 m from the intersection point. The material traversed by a charged particle before entering the drift chamber amounts to 0.045 radiation lengths, coming predominantly from the stainless-steel beam pipe (at 12 cm) and an inner scintillator hodoscope (at 18 cm).

The drift chamber is described in detail elsewhere [5]. Briefly, it is a single-gas-volume chamber operating at atmospheric pressure with a mixture of argon (50%) + ethane (50%). Each half chamber (fig. 1) consists of 41 sectors, of 4° width, leaving dead regions of 8° width up and down in azimuth. Each sector has 42 radially distributed sense wires oriented parallel to the magnetic field, and

organized into three groups or 'crowns'. The wires are staggered ± 0.4 mm azimuthally to remove left-right ambiguities. The drift-time information is complemented by pulse heights recorded from both ends of the sense wires and used to obtain the position along the wire by charge division as well as the particle identity by ionization. The drift times give an average resolution of 230 μm , and the charge division ~ 1.5 cm, after correcting for effects such as bending of the electron drift paths by the magnetic field, differences in electronic delays, and time-slewing effects caused by finite thresholds in the electronics. The resulting momentum resolution in the central part of the drift chamber is given approximately by $\delta p/p = \sqrt{(0.025p)^2 + (0.01)^2}$ (p in GeV/c), where the first term comes from measurement errors and the second from multiple scattering in the chamber gas and wires.

The event time was recorded using the cylindrical scintillator hodoscope, placed between the vacuum pipe and the drift chamber. Timing on the inner hodoscope is also used to reject multiple events, occurring within the read-out window of ± 600 ns. Two sets of scintillators were placed in the forward regions ($1.2^\circ < \theta < 6^\circ$) to monitor the luminosity and for use in the trigger. The trigger required a coincidence between these forward counters or a hit in the central scintillator hodoscope (minimum bias trigger). This trigger records $\sim 90\%$ of the inelastic cross-section.

3. DATA ANALYSIS

This analysis is based on $\sim 2 \times 10^5$ triggers as defined in the previous section. The luminosity was 2×10^{31} $\text{cm}^{-2} \text{s}^{-1}$ during data taking. The events were passed through a track-reconstruction program, which found track candidates in space (r, ϕ, z). Events containing at least one track candidate were then passed through a fitting program to determine the track parameters, using the spline method [6]. The track parameters and errors were then used to estimate a common event vertex position, and associate a subset of all reconstructed and fitted tracks with the event. From the initial sample, 9×10^4 events contained a vertex.

All tracks in the remaining sample were required to originate from the event vertex, and contain 10 or more space points. These cuts were necessary to reduce

contamination from background sources such as beam-pipe interactions, upstream beam-gas interactions and old hits in the drift chambers. In addition, we required a $\chi^2/\text{degree of freedom} < 3.0$ for the single-track fits. This was particularly useful for rejecting errors introduced earlier at the track-reconstruction stage. A final selection was applied on the measurement errors of the individual track parameters.

Particles in this sample were identified using the information on the ionization from the drift chamber. The ionization for a track was defined as the mean value of the lower 70% of the individual pulse heights. Figure 2 shows the truncated mean pulse height versus track momentum for negative particles. Each particle type appears clearly. Particles were defined as kaons in a region of this plot where the contamination from other particles is $< 5\%$.

The single-particle acceptance as a function of particle type (either kaon or any hadron), charge, rapidity, p_T , and azimuth for the observed particles was deduced by comparing their densities with previously measured spectra [7]. The detection efficiency with the chosen cuts for all hadrons rises to a level of $\sim 50\%$ for $p_T > 300$ MeV/c and remains approximately constant. Kaon efficiencies rise to a peak value of $\sim 40\%$ at a p_T of ~ 400 MeV/c, and drop to zero at approximately 700 MeV/c, as dE/dx separation fails. We estimate the systematic uncertainty in acceptance introduced by this technique to be 15% and 5% for kaons and hadrons, respectively. These errors arise predominantly from the normalization and our representation of the previous measurements.

To translate these single-particle acceptances into detection efficiencies for two-body vector-meson decays, we employed a Monte Carlo technique. Vector mesons were generated with a P-wave Breit-Wigner distribution. They were assumed to be produced unpolarized, with y and p_T distributions consistent with the measured differential cross-sections quoted later. It was checked that there was no azimuthal variation of the vector mesons and that the decay was indeed isotropic. The momenta of the decay particles were smeared with the detector resolution. The vector meson was then given a weight equal to the product of the acceptances derived from the

single-particle acceptance tables. The resulting vector-meson acceptances are shown in figs. 3a-f for ρ^0 , K^{*0} , and ϕ , as a function of p_T and y . The acceptance calculated from uncorrelated single-particle spectra does not fully account for losses in the detector introduced by the two-body kinematics of the decays. We have estimated such effects to be $< 1\%$, $< 1\%$, and $\sim 4\%$ for ρ , K^* , and ϕ , respectively, and have included these uncertainties in our acceptance errors.

The invariant masses of $\pi^+\pi^-$ and $K^+\pi^+$ were formed. The mass spectra are shown in figs. 4a and 5a, where the solid line represents the shape of the uncorrelated background determined by combining particles from alternate events of the same multiplicity. Background shapes constructed in this way also agree well for $\pi^+\pi^+$ combinations. For ρ^0 and K^{*0} , the background-shape normalization was chosen to remain positive in the regions surrounding the signals after subtraction. For the ρ^0 this was obtained by normalizing above $2 \text{ GeV}/c^2$, while for the K^* the lack of statistics in the high-mass tail of the $K\pi$ spectrum forced an arbitrary normalization. The resulting spectra are shown in figs. 4b and 5b, where prominent ρ^0 and K^{*0} signals appear.

A fit to each subtracted mass distribution was performed using a P-wave Breit-Wigner formula with nominal mass and width, together with an assumed exponential non-resonant correlation background in the ρ^0 case, and a linear form for the K^{*0} . We have found that the shape uncertainties in resonance and background forms lead to changes of less than 15% and 4% in the ρ^0 and K^{*0} signals, respectively, while still retaining acceptable fits.

Figure 6 shows the K^+K^- invariant mass spectrum. The ϕ resonance is well fit by a Breit-Wigner of width $10 \text{ MeV}/c^2$ (consistent with the detector resolution) and a constant background.

4. RESULTS

The distributions of produced resonances have been studied as a function of transverse mass (μ_T) and rapidity (y). In determining absolute cross-sections, we have included in the tables an overall systematic uncertainty of 20%, coming

from our luminosity measurement (7%) and event selection criteria, in addition to the acceptance and fitting errors. However, the errors shown in the figures are purely statistical.

The cross-sections as a function of μ_T are summarized in tables 1 to 4 and displayed in fig. 7. The inclusive spectrum for each resonance is well fitted by a simple exponential

$$E \frac{d^3\sigma}{dp^3} \propto \exp(-a\mu_T) ,$$

with $a = 6.4 \pm 0.2 \text{ GeV}^{-1}$. The data can also be fitted to similar exponentials in p_T and p_T^2 . The results of these fits are presented in table 5. We see from fig. 7 that the μ_T distribution for the ρ^0 is in agreement with the previous measurements of ref. 1, at the same centre-of-mass energy, but rescaled to the same rapidity region.

The centre-of-mass rapidity distributions for ρ^0 , K^* , and ϕ are shown in fig. 8, and summarized in tables 1 to 4. The data are consistent with no variation with rapidity over the range covered by this experiment.

The ratio of $\langle \rho^0 \rangle / \langle \pi^- \rangle$ is shown in fig. 9 as a function of p_T . The rise of this curve from ~ 0.0 at low p_T levels to a level of ~ 0.7 at $p_T \sim 1.2 \text{ GeV}/c$ appears to be approaching the similarly high ratio of 0.87 ± 0.17 previously measured for $\langle \omega \rangle / \langle \pi^0 \rangle$ at $\sqrt{s} = 63 \text{ GeV}$ with $p_T > 3$ and $y = 0$ [8]. In addition, the following particle ratios have been extracted from the data, in the range $p_T < 1.5$, $|y| < 1$:

$$\begin{aligned} \langle \rho^0 \rangle / \langle \pi^- \rangle &= 0.20 \pm 0.03 \pm 0.04 \\ \langle K^* \rangle / \langle K^- \rangle &= 0.64 \pm 0.09 \pm 0.03 \\ \langle \bar{K}^* \rangle / \langle K^+ \rangle &= 0.55 \pm 0.08 \pm 0.03 \\ \langle \phi \rangle / \langle \rho^0 \rangle &= 0.09 \pm 0.02 \pm 0.02 , \end{aligned}$$

where the first error is statistical and the second is systematic. These particle ratios are shown in figs. 10 and 11, together with lower energy data covering larger rapidity. The dashed lines in these plots indicate a quark-model prediction based on spin statistics. Assuming isospin invariance and equal production of ρ^0 and ω , the above ratios imply that $\sim 60\% \pm 15\%$ of all pseudoscalar mesons are decay products of vector mesons.

Acknowledgements

We acknowledge with thanks the work of the CERN Experimental Facilities Division on the drift chamber construction, and that of the Experimental Support Group of the ISR Division who installed the experiment.

Support from the Research Councils in our home countries is gratefully acknowledged.

REFERENCES

1. M.G. Albrow et al., Nucl. Phys. B155 (1979) 39.
D. Drijard et al., Z. Phys. C9 (1981) 293.
2. V. Blobel et al., Phys. Lett. 48B (1974) 73.
V.V. Ammosov et al., Sov. J. Nucl. Phys. 24 (1976) 30.
C. Daum et al., Nucl. Phys. B186 (1981) 205.
M. Schouten et al., Z. Phys. C9 (1981) 93.
R. Singer et al., Phys. Lett. 60B (1976) 385.
R. Singer et al., Nucl. Phys. B135 (1978) 265.
H. Kichimi et al., Phys. Rev. D 20 (1979) 37.
A. Suzuki et al., Lett. Nuovo Cimento 24 (1979) 449.
H. Kichimi et al., Lett. Nuovo Cimento 24 (1979) 129.
K. Böckmann, Proc. EPS Int. Conf. on High-Energy Physics, Palermo, 1975
(Editrice Compositori, Bologna, 1976), p. 794.
D. Morrison, preprint CERN-EP/79-102 (1979).
3. V.V. Anisovich and V.M. Shekhter, Nucl. Phys. B55 (1973) 455.
V.M. Shekhter and L.M. Shcheglova, Sov. J. Nucl. Phys. 27 (1978) 567.
4. S. Nandi, V. Rittenberg and H.R. Schneider, Phys. Rev. D 17 (1978) 1336.
K.V. Vasavada, Phys. Rev. D 20 (1979) 2304.
5. D. Cockerill et al., Nucl. Instrum. Methods 176 (1980) 159.
6. S. Almeded and B. Lorstad, Comput. Phys. Commun. 22 (1981) 209.
7. B. Alper et al., Nucl. Phys. B100 (1975) 237.
K. Guettler et al., Nucl. Phys. B116 (1976) 77.
8. M. Diakonou et al., Phys. Lett. 89B (1980) 432.

Table 1

ρ^0 data

a) Cross-section versus p_T

p_T (GeV/c)	$\langle p_T \rangle$ (GeV/c)	$\langle \mu_T \rangle$ (GeV/c)	$E(d^3\sigma/dp^3)$ (mb/GeV ²)	χ^2/NDF
0.00-0.25	0.17	0.79	$7.8 \pm 0.8 \pm 1.4$	33/25
0.25-0.50	0.38	0.86	$3.85 \pm 0.41 \pm 0.69$	31/25
0.50-0.75	0.62	0.99	$1.94 \pm 0.19 \pm 0.35$	30/25
0.75-1.00	0.86	1.15	$0.64 \pm 0.09 \pm 0.12$	26/28
1.00-1.50	1.15	1.37	$0.17 \pm 0.02 \pm 0.03$	29/25

b) Cross-section versus y

y	$d\sigma/dy$ (mb)	χ^2/NDF
0.00-1.00	$6.5 \pm 0.8 \pm 1.2$	29/25
0.00-0.33	$6.8 \pm 1.0 \pm 1.2$	22/25
0.33-0.67	$6.7 \pm 0.6 \pm 1.2$	27/25
0.67-1.00	$5.3 \pm 0.9 \pm 1.0$	18/25

Table 2

K*⁰ data

a) Cross-section versus p_T

p _T (GeV/c)	⟨p _T ⟩ (GeV/c)	⟨μ _T ⟩ (GeV/c)	E(d ³ σ/dp ³) (mb/GeV ²)	χ ² /NDF
0.00-0.25	0.17	0.91	1.97 ± 0.51 ± 0.35	22/18
0.25-0.50	0.38	0.97	0.96 ± 0.23 ± 0.17	26/18
0.50-0.75	0.62	1.08	0.65 ± 0.16 ± 0.12	17/18
0.75-1.00	0.86	1.24	0.26 ± 0.07 ± 0.05	23/18
1.00-1.50	1.15	1.45	0.033 ± 0.022 ± 0.006	17/18

b) Cross-section versus y

y	dσ/dy (mb)	χ ² /NDF
0.00-1.00	1.94 ± 0.28 ± 0.35	22/18
0.00-0.33	2.26 ± 0.37 ± 0.41	15/18
0.33-0.67	1.45 ± 0.47 ± 0.26	17/18

Table 3

\bar{K}^{*0} data

a) Cross-section versus p_T

p_T (GeV/c)	$\langle p_T \rangle$ (GeV/c)	$\langle \mu_T \rangle$ (GeV/c)	$E(d^3\sigma/dp^3)$ (mb/GeV ²)	χ^2/NDF
0.00-0.25	0.17	0.91	1.41 ± 0.51 ± 0.25	23/18
0.25-0.50	0.38	0.97	1.12 ± 0.23 ± 0.20	20/18
0.50-0.75	0.62	1.08	0.52 ± 0.16 ± 0.09	16/18
0.75-1.00	0.86	1.24	0.16 ± 0.07 ± 0.03	9/18
1.00-1.50	1.15	1.45	0.050 ± 0.024 ± 0.009	23/18

b) Cross-section versus y

y	$d\sigma/dy$ (mb)	χ^2/NDF
0.00-1.00	1.87 ± 0.28 ± 0.34	23/18
0.00-0.33	2.22 ± 0.39 ± 0.40	15/18
0.33-0.67	1.43 ± 0.38 ± 0.26	32/18

Table 4

ϕ data

a) Cross-section versus p_T

p_T (GeV/c)	$\langle p_T \rangle$ (GeV/c)	$\langle \mu_T \rangle$ (GeV/c)	$E(d^3\sigma/dp^3)$ (mb/GeV ²)
0.25-0.50	0.38	1.09	$0.22 \pm 0.12 \pm 0.05$
0.50-0.75	0.62	1.19	$0.17 \pm 0.05 \pm 0.04$
0.75-1.00	0.86	1.33	$0.061 \pm 0.023 \pm 0.015$
1.00-1.50	1.15	1.53	$0.023 \pm 0.011 \pm 0.006$

b) Cross-section versus y

y	$d\sigma/dy$ (mb)
0.00-1.00	$0.58 \pm 0.12 \pm 0.13$
0.00-0.33	$0.44 \pm 0.11 \pm 0.10$
0.33-0.67	$0.55 \pm 0.22 \pm 0.12$

Table 5

Results^{a)} of fits to the cross-sections

Fit	A exp (-a t _T)		B exp (-b t _T)		C exp (-c t _T)				
	A (mb)	a (GeV ⁻¹)	χ ² /NDF	B (mb)	b (GeV ⁻¹)	χ ² /NDF	C (mb)	c (GeV ⁻²)	χ ² /NDF
ρ ⁰	1083 ± 55	6.4 ± 0.3	2.8/3	16.6 ± 0.8	3.9 ± 0.1	7.8/3	6.5 ± 0.3	3.0 ± 0.1	10/3
K* ⁰	671 ± 87	6.6 ± 0.8	2.3/3	4.0 ± 0.9	3.7 ± 0.4	4.0/3	1.7 ± 0.3	2.9 ± 0.4	1.7/3
\bar{K}^{*0}	573 ± 52	6.5 ± 1.0	0.3/3	3.5 ± 0.8	3.5 ± 0.4	2.6/3	1.6 ± 0.3	2.9 ± 0.5	0.6/3
φ	103 ± 15	5.5 ± 1.4	0.4/2	0.91 ± 0.56	3.1 ± 0.7	0.8/2	0.33 ± 0.13	2.1 ± 0.6	0.4/2
ρ ⁰	1085 ± 265			16.0 ± 1.4			6.33 ± 0.3		
K* ⁰	561 ± 162	6.4 ± 0.2	0.6/14	4.0 ± 0.6	3.8 ± 0.1	17/14	1.6 ± 0.2	2.9 ± 0.1	14/14
\bar{K}^{*0}	532 ± 155			4.3 ± 0.6			1.7 ± 0.2		
φ	321 ± 114			1.4 ± 0.3			0.48 ± 0.10		

a) The errors in A, B, and C are statistical only and do not contain possible normalization errors of 7%.

Figure captions

- Fig. 1 : a) Schematic drawing of the Axial Field Magnet and the vertex drift chamber.
b) End view of the drift chamber.
c) Expanded view of a sector structure. The staggering of the sense wires, shown as crosses, has been exaggerated by a factor of five.
- Fig. 2 : dE/dx identification: truncated mean pulse height versus the momentum for negative particles. The contours represent a factor 2 in density.
- Fig. 3 : Vector-meson acceptances as a function of p_T and rapidity: a) ρ^0 ;
b) K^{*0} ; c) ϕ .
- Fig. 4 : $\pi^+\pi^-$ invariant mass spectra.
a) Combinations within the same event. The full line describes the non-resonant background determined by mixing events.
b) The background-subtracted signal. Fitted curves are described in the text.
- Fig. 5 : $K^+\pi^-$ invariant mass spectra.
a) Combinations within the same event. The full line describes the non-resonant background determined by mixing events.
b) The background-subtracted signal. Fitted curves are described in the text.
- Fig. 6 : K^+K^- mass spectra for all combinations. The curve is a fit to a Breit-Wigner together with a constant background.
- Fig. 7 : $E(d^3\sigma/dp^3)$ as a function of transverse mass (μ_T) for ρ^0 , K^{*0} , \bar{K}^{*0} , and ϕ . The lines represent a global fit of the form $\exp(-a\mu_T)$.
- Fig. 8 : Rapidity distributions $d\sigma/dy$: a) ρ^0 ; b) K^{*0} ; c) ϕ .
- Fig. 9 : p_T dependence of ρ/π^- .

Fig. 10 : ρ/π^- as a function of \sqrt{s} : ● - this experiment; ○ - refs. 1,2.

Fig. 11 : a) K^*/K as a function of \sqrt{s} . ■ K^*/K^- , ● \bar{K}^*/K^+ - this experiment;
□ K^{*-}/K_S^0 , ○ K^{*+}/K_S^0 - ref. 2.

b) ϕ/ρ as a function of \sqrt{s} : ● - this experiment; ○ - ref. 2. The dashed lines are predictions from ref. 3 for the central region.

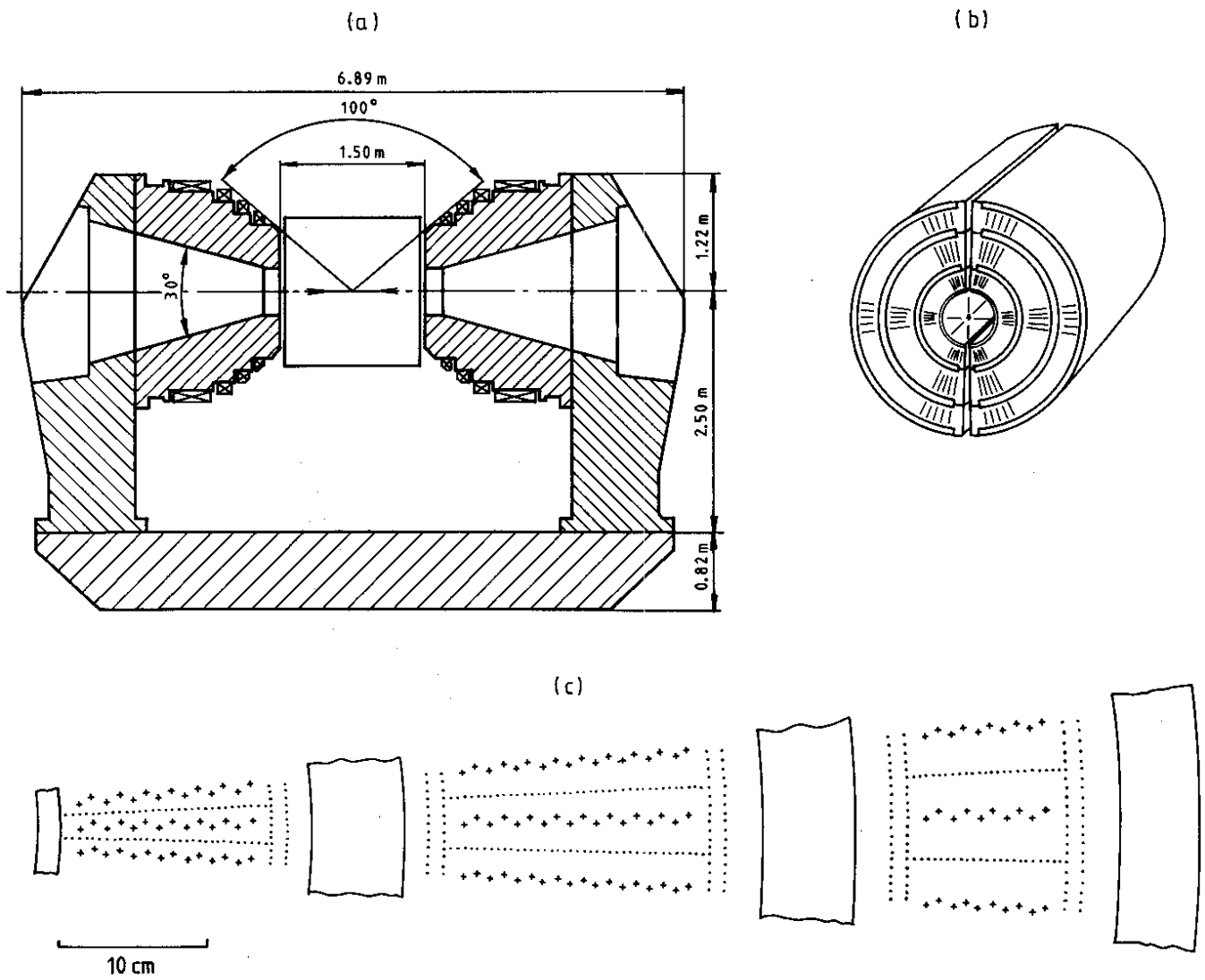


Fig. 1

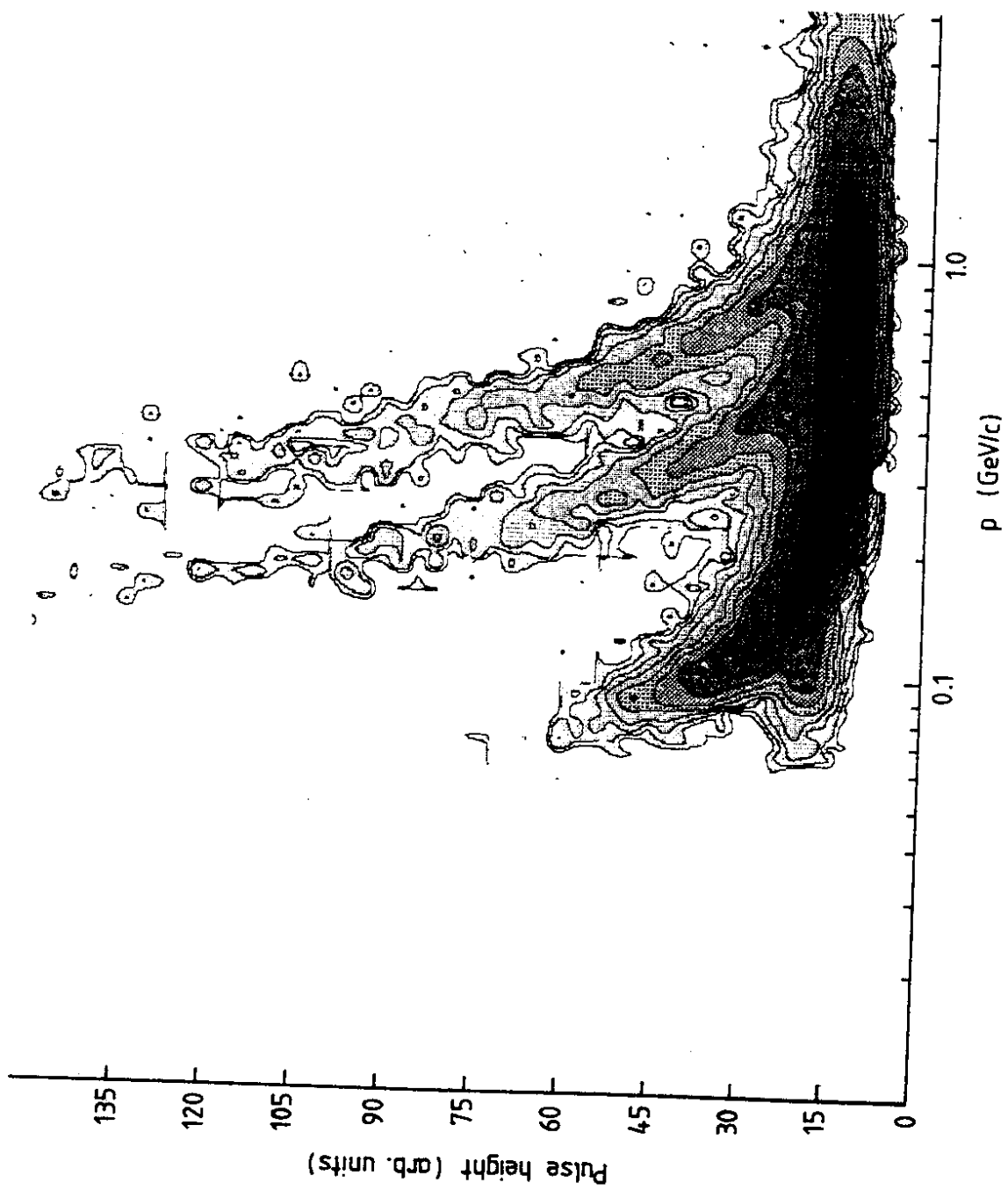


Fig. 2

Vector - meson acceptance

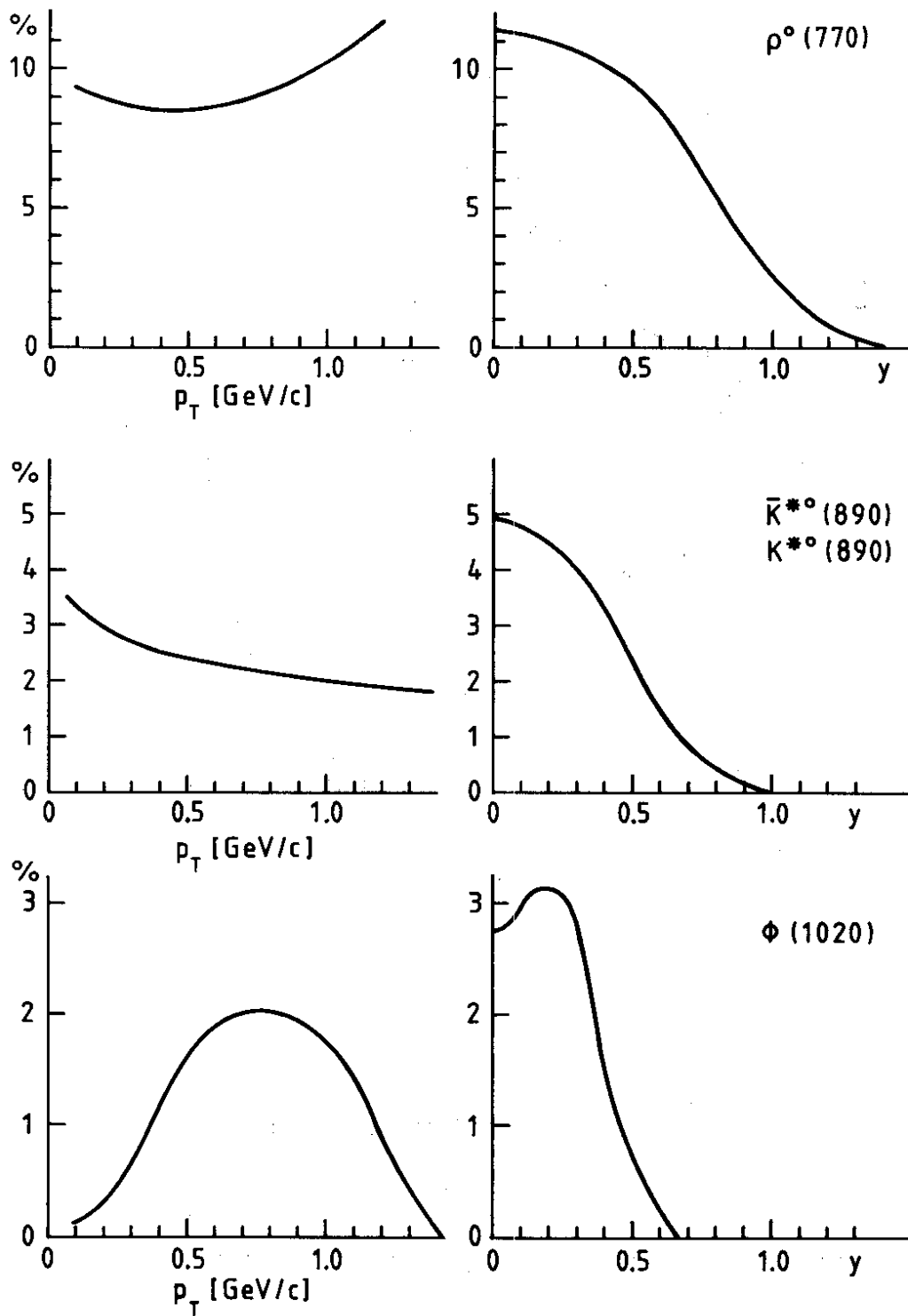


Fig. 3

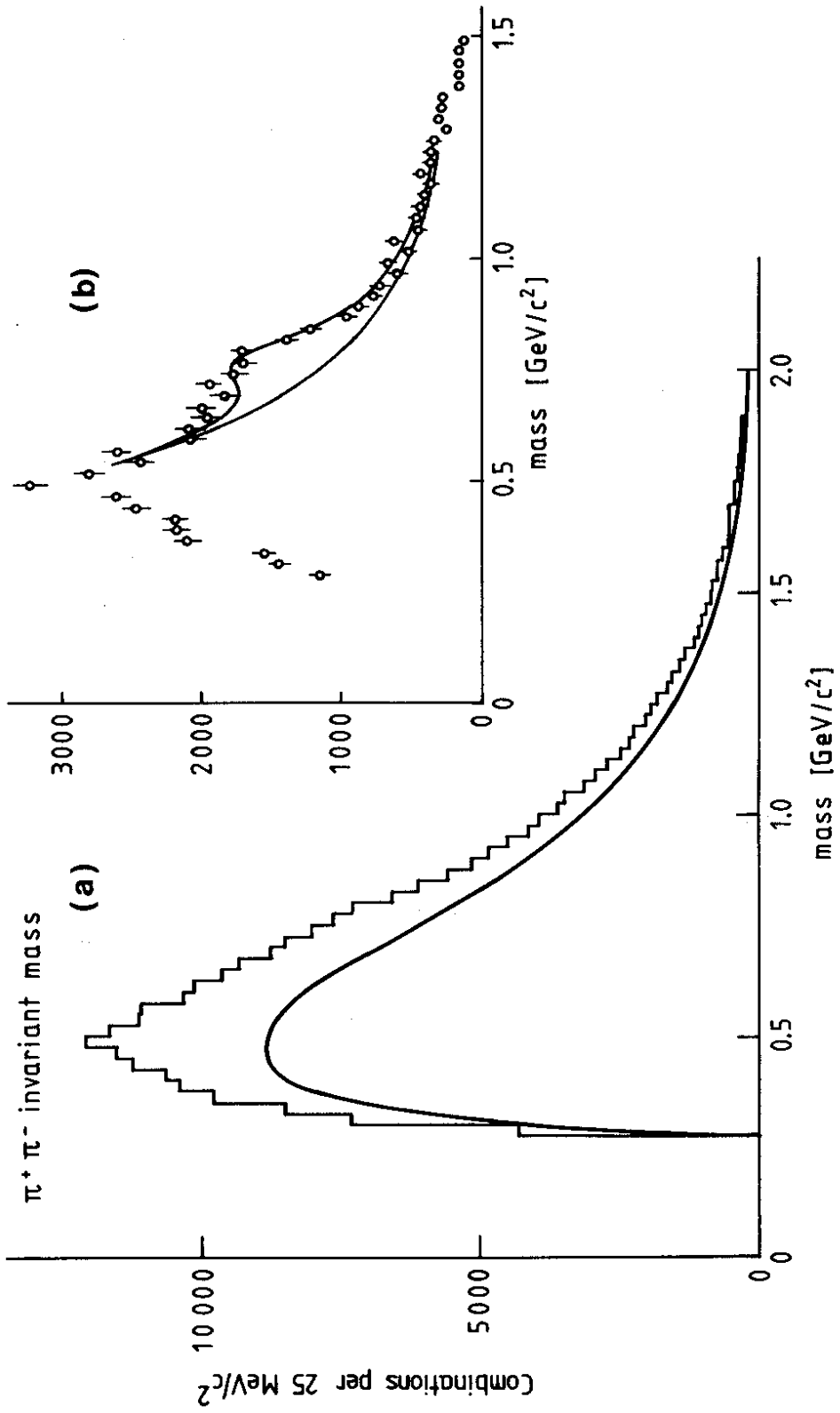


Fig. 4

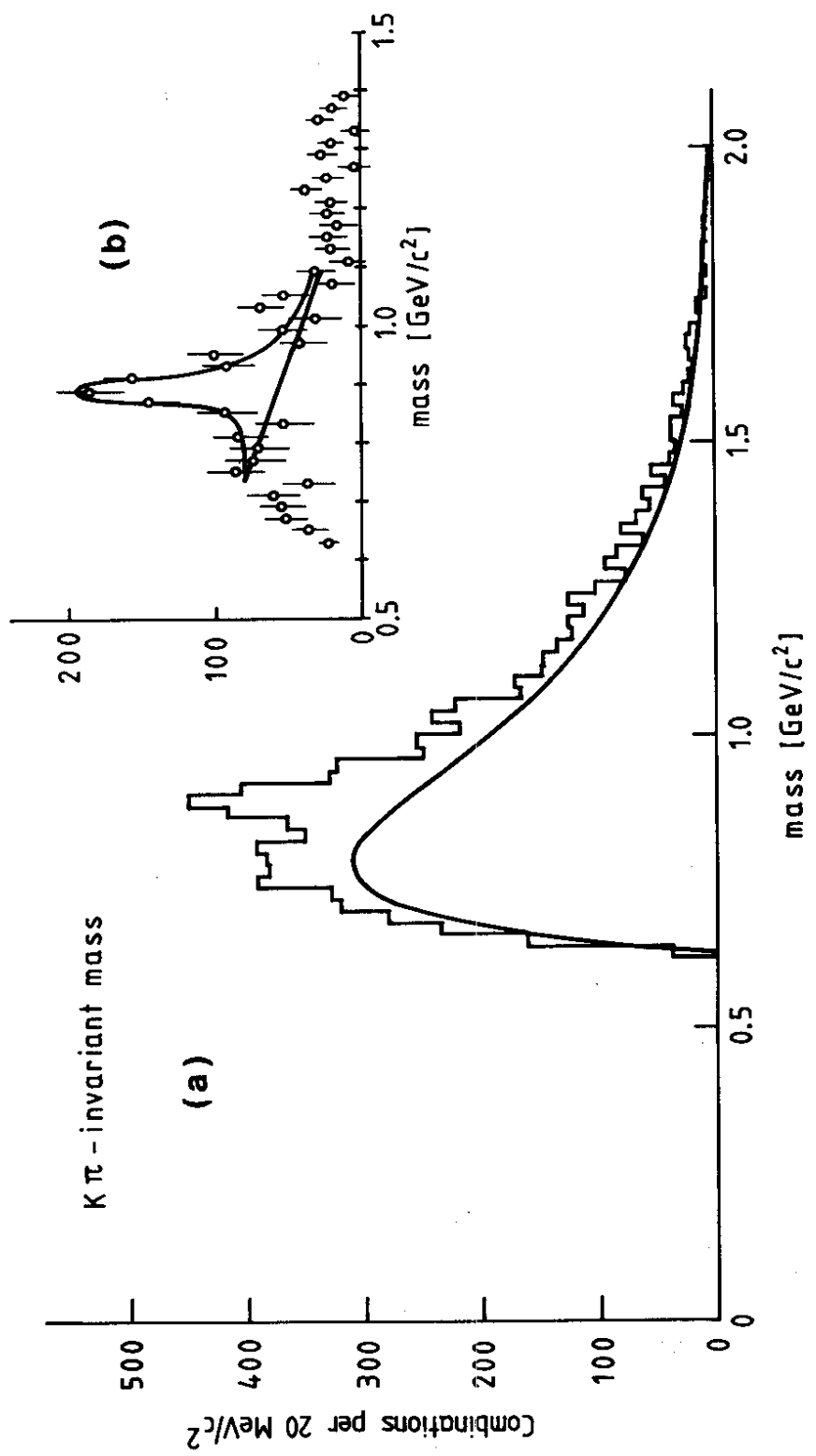


Fig. 5

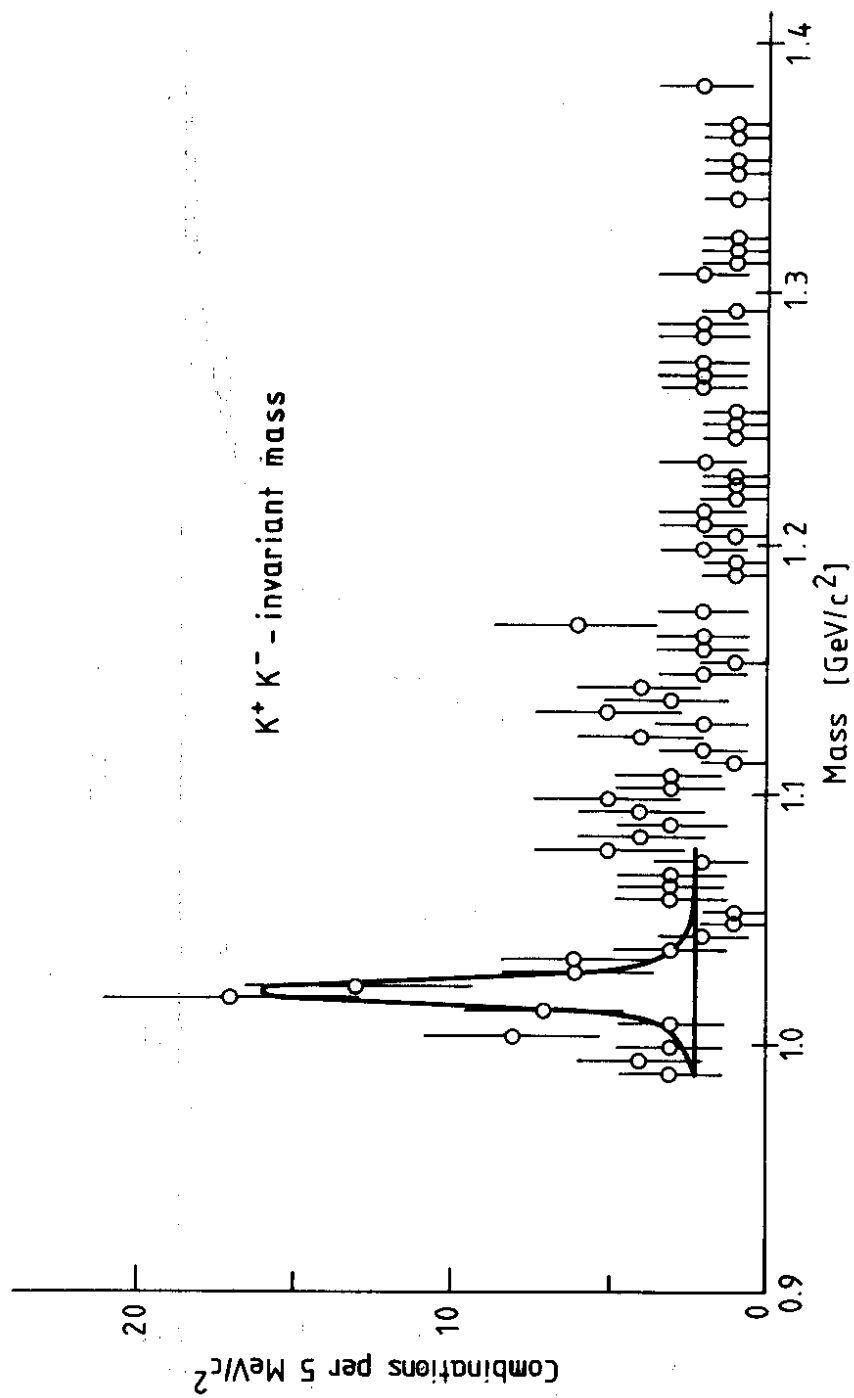


Fig. 6

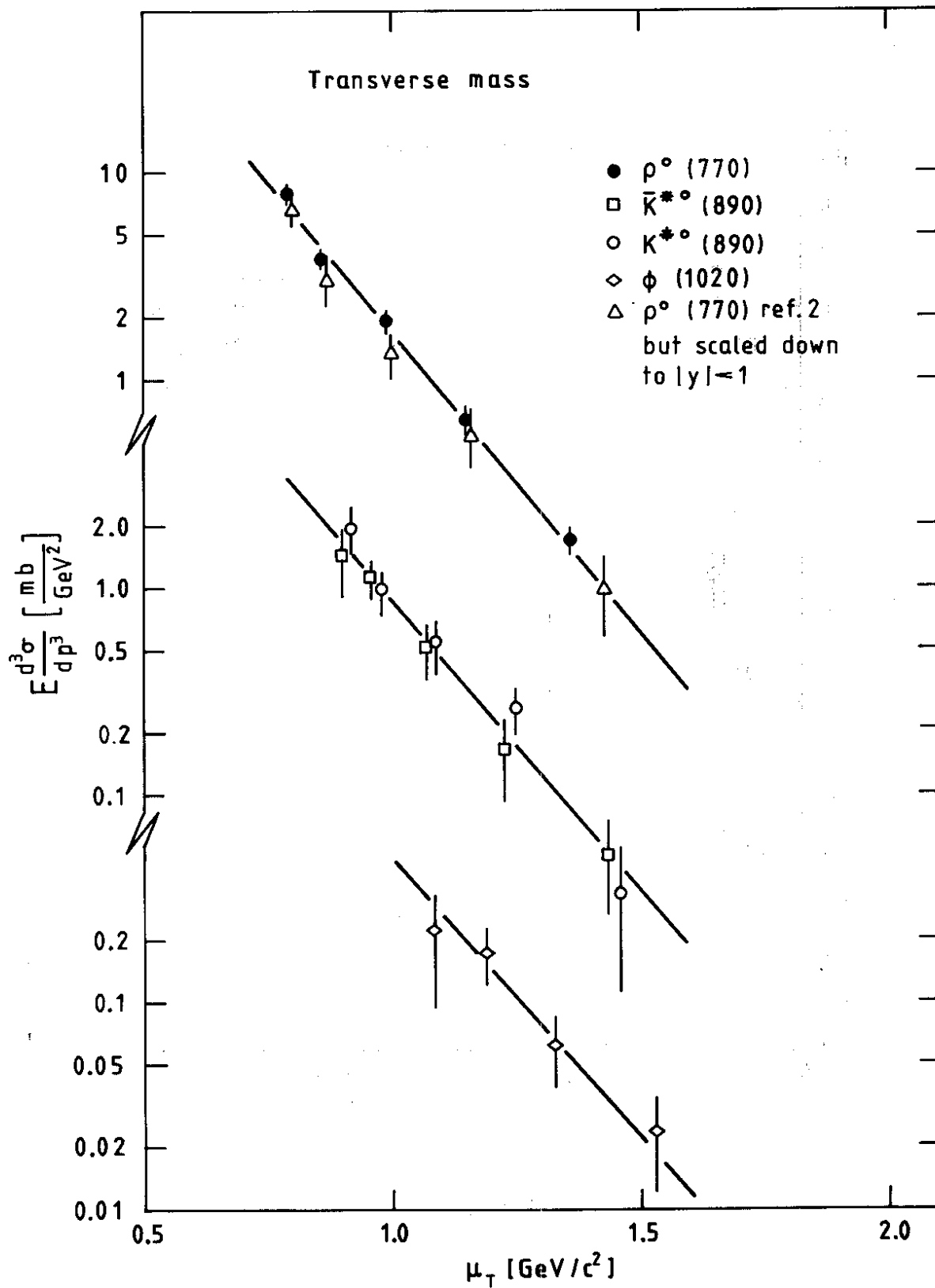


Fig. 7

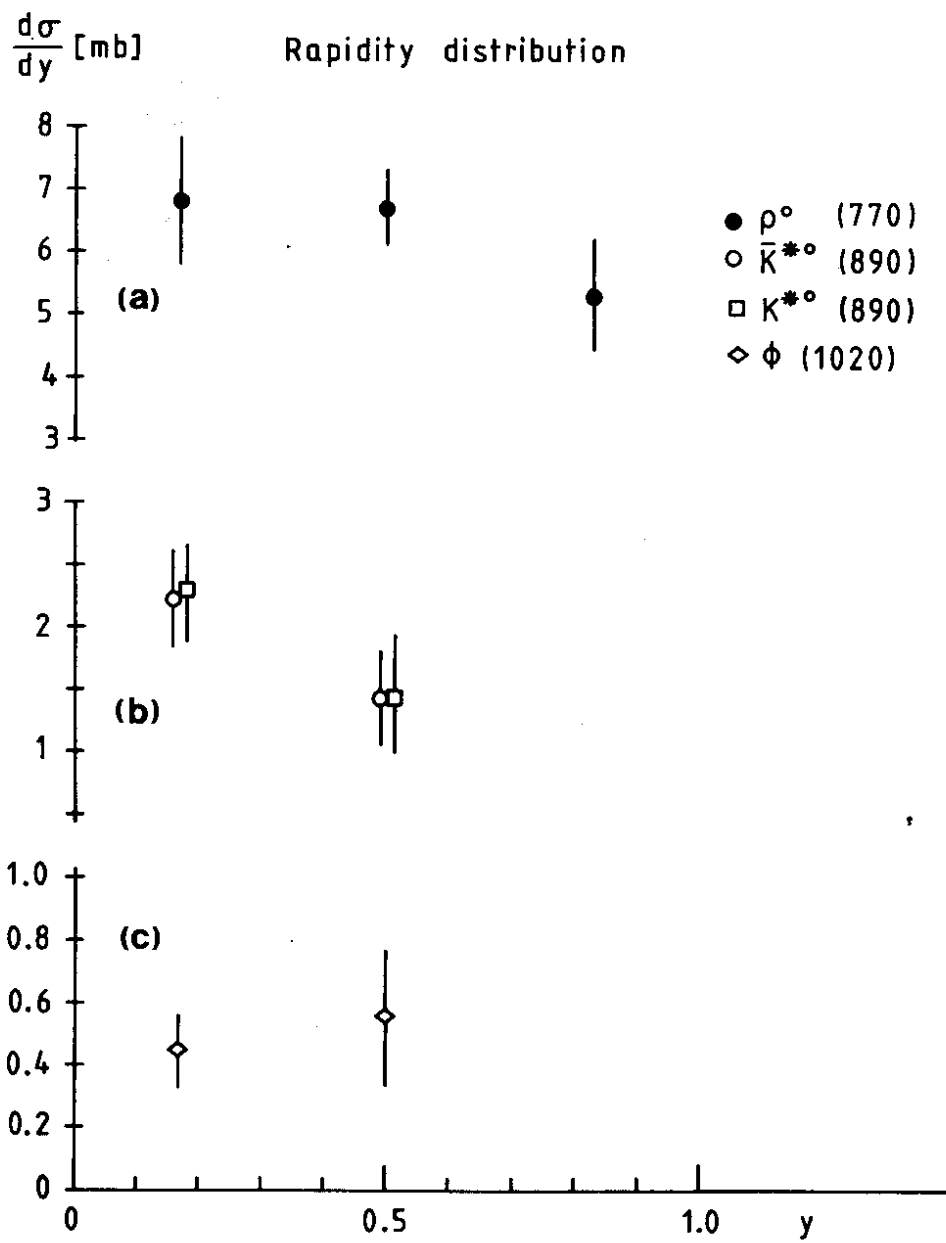


Fig. 8

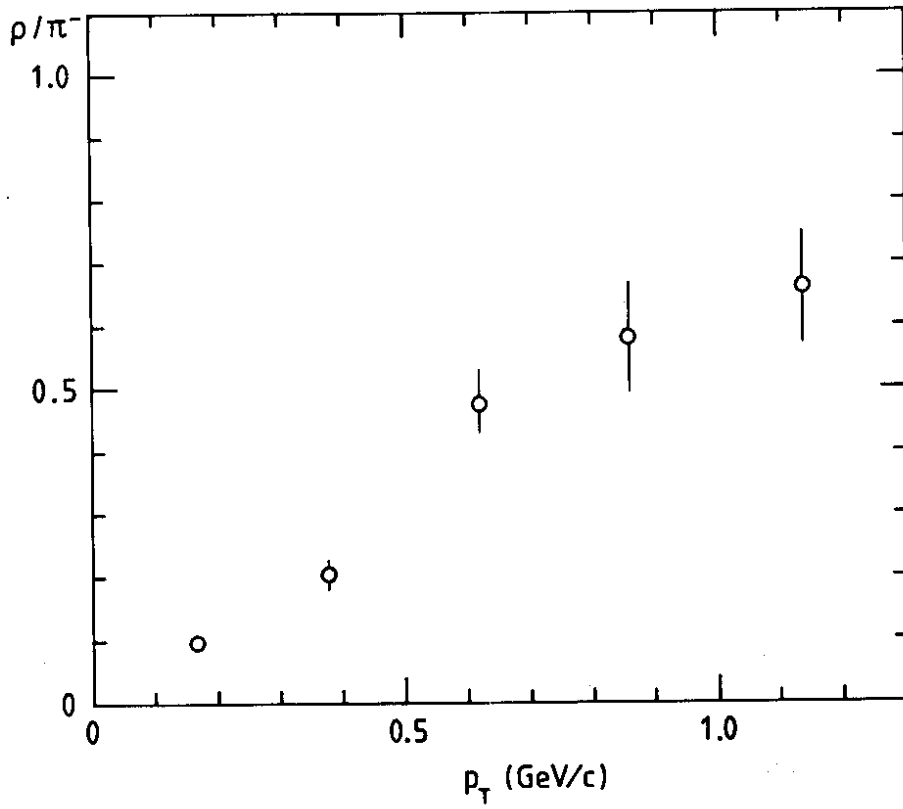


Fig. 9

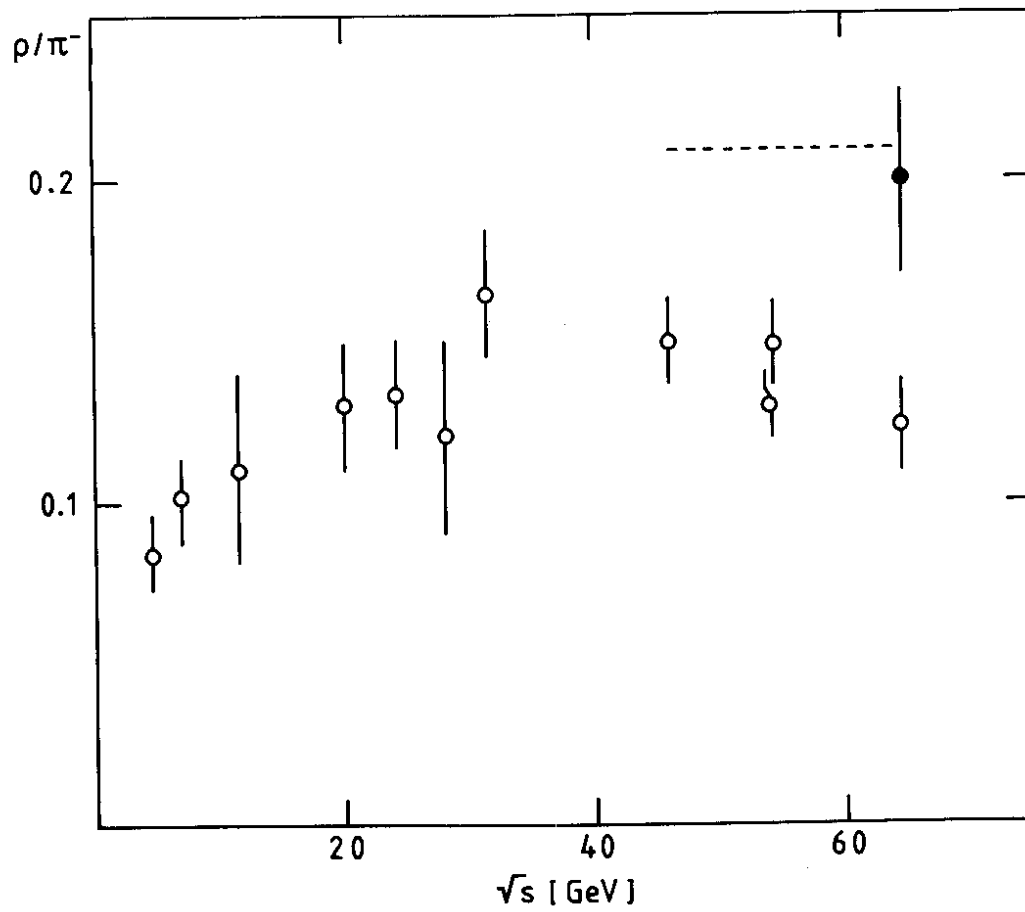


Fig. 10

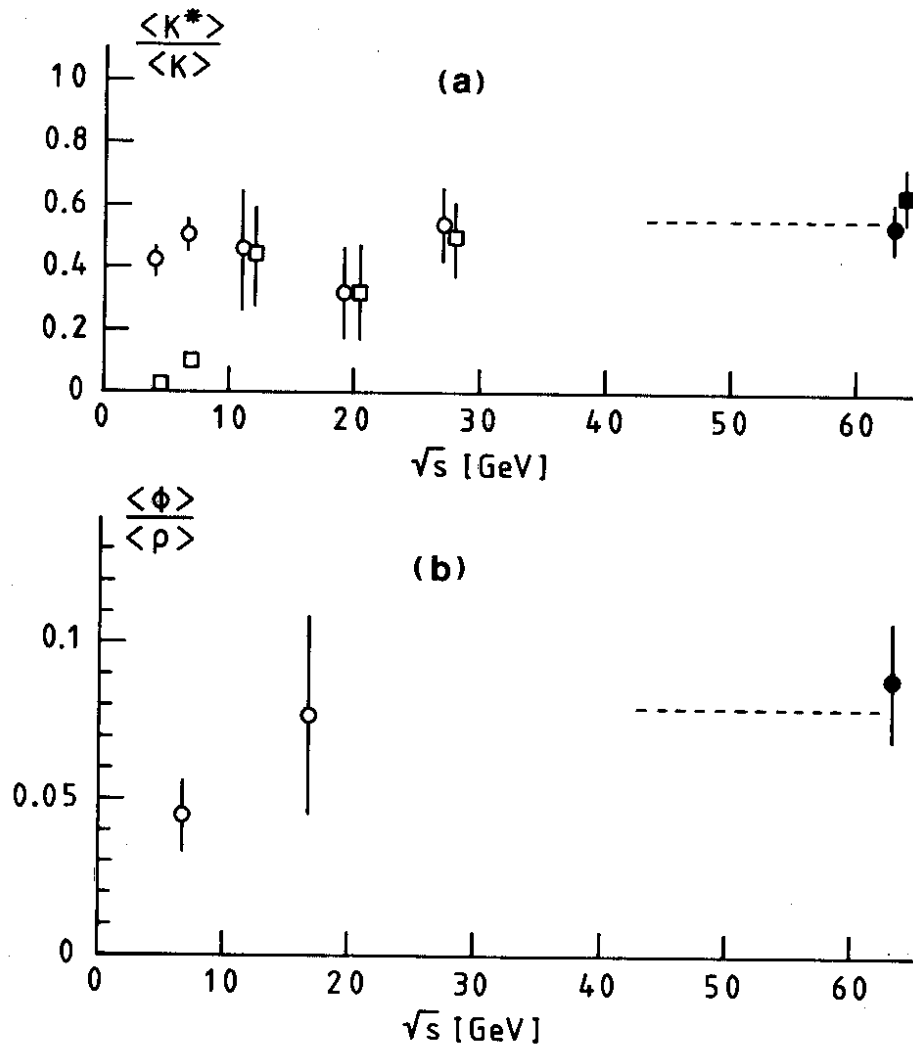


Fig. 11